

Neurodegenerative damage reduces firing coherence in a continuous attractor model of grid cells

Yuduo Zhi* and Daniel Cox†

Physics Department, University of California, Davis

(Dated: August 12, 2020)

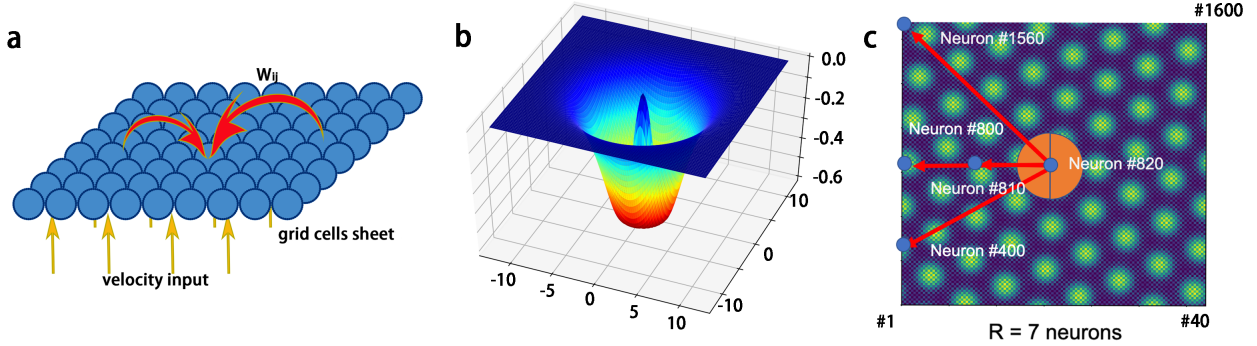


FIG. 1. **2D neuron sheet and damage model (after Ref. 2).** (a) Blue spheres are neurons in the grid cell model, and red arrows indicate synaptic connections among neurons, with a weight W_{ij} coupling neuron i and neuron j . The yellow arrows below are the velocity signal from other cells. The instantaneous velocity input is uniform for the grid cell sheet, but each cell has a different preferred direction. (b) The "Mexican Hat" weight matrix W_{ij} is the difference between two Gaussians. It is negative everywhere except at the center (zero). (c) Central damage model. The heatmap indicates the 40×40 grid cell layer firing peaks, with the orange circle indicating the damaged region (radius $R = 7$ neurons in this case). All neurons are numbered from 1 to 1600, and the neuron at the damage center is #820.

Abstract

Grid cells in the dorsolateral band of the medial entorhinal cortex(dMEC) display strikingly regular periodic firing patterns on a lattice of positions in 2-D space. This helps animals to encode relative spatial location without reference to external cues. The dMEC is damaged in the early stages of Alzheimer's Disease, which affects navigation ability of a disease victim, reducing the synaptic density of neurons in the network. Within an established 2-dimensional continuous attractor neural network model of grid cell activity, we introduce damage parameterized by radius and by the strength of the synaptic output for neurons in the damaged region. The proportionality of the grid field flow on the dMEX to the velocity of the model organism is maintained, but when we examine the coherence of the grid cell firing field in the form of the Fourier transform (Bragg peaks) of the grid lattice, we find that a wide range of damage radius and strength induces an incoherent structure with only a single central peak, adjacent to narrow bands of striped (two additional peaks), which abut an orthorhombic pattern (four additional peaks), that abuts the undamaged hexagonal region (six additional peaks). Within the damaged region, grid cells show no Bragg

peaks, and outside the damaged region the central Bragg peak strength is largely unaffected. There is a re-entrant region of normal grid firing for very large damage area. We anticipate that the modified grid cell behavior can be observed in non-invasive fMRI imaging of the dMEC.

I. INTRODUCTION

There is considerable interest in understanding how the brain encodes location and guides animal navigation. Different neural networks within the brain with various functions help to build animals' navigation system. For instance, place cells in the hippocampus are confirmed to fire strongly at special locations such as reward sites or for the position of external landmarks[1, 2]. Head-direction cells found in many brain areas (e.g., the dorsal presubiculum)[3] fire in 1:1 correspondence with the animal's directional heading with respect to the environment in the horizontal plane[4, 5]. The stunning discovery of grid cells in 2005 showed that these neurons in the dorsocaudal medial entorhinal cortex (dMEC) provide an internal coordinate system encoding absolute position for a given enclosure (longitude and latitude) largely independent of external environmental cues[6, 7]. Each grid cell in a given layer of the dMEC shows enhanced activity (firing) on a periodic hexagonal lattice of points in 2-D space, with the spacing varying with layer depth.

Alzheimer's disease (AD) strongly affects the hippocampus (place cells) and entorhinal cortex (grid cells) and thus can disrupt spatial navigation. Several competing hypotheses exist to explain the cause of the disease. The "tau hypothesis", proposes that abnormalities associated with tau protein aggregates initiate the disease cascade[8]. In this model, hyperphosphorylated tau does not hold microtubules together and begins to pair with other threads of tau to form neurofibrillary tangles inside nerve cell bodies[9]. Because the tau protein is what stabilizes the microtubule bundles in neuronal axons on which neurotransmitters and other cargoes relevant for normal synaptic function are transported, this may result first in malfunctions in biochemical communication at the synapses between neurons and later in the death of the cells[10]. Furthermore, the tau tangles that disrupt the axon and synapses may propagate within the brain from location to location, in a manner similar to the prion protein aggregates of mad cow disease[11–13]. The other leading candidates

* ydzhi@ucdavis.edu

† cox@physics.ucdavis.edu

for initiation of Alzheimer's disease, the "amyloid cascade" hypothesis[14], or the related "amyloid oligomer" hypothesis[15], lead to eventual tau aggregation as well as an end stage.

There is substantial direct evidence for AD related damage to the MEC. Direct post-mortem examination shows significant atrophy of the EC in the brains of AD victims vs. control[16]. fMRI imaging of the MEC region for patients predisposed to early onset AD shows a disruption in the six-fold symmetric firing pattern with respect to the control group when performing virtual navigation tasks, despite no apparent cognitive deficits in the AD disposed group[17]. Similar works on aging adults suggests an impact of AD on the grid cell function and ability to navigate[18]. Amyloid beta oligomers induce tau tangles in cell culture experiments that degrade microtubules and synaptic quality[19]. Overexpression of human tau protein with subsequent aggregation in rats leads to degradation of synaptic plasticity in the MEC and degrades cognitive performance[20], and induced expression of mutant human tau in mice leads to grid cell dysfunction[21]. Finally, there is direct evidence of AD induced synaptic degradation in the neurons projecting from the MEC to the CA1 layer of the hippocampus[22].

In this paper, we analyze the impact to animal navigation caused by grid cell damage via neurodegeneration, in which we assume that the synaptic strength of output connection, α , with $0 \leq \alpha \leq 1$, for neurons in a circular disk of radius R , are degraded presumably due to the tau tangle influence on the synaptic cargo transport and degradation of microtubules. Within the continuous attractor model for grid cells introduced by Burak and Fiete[23], we find that the damage does not influence the key proportionality between firing flow and animal velocity necessary to achieve path integration and a hexagonal lattice firing pattern, but rather disrupts the coherent pattern of grid cell firing yielding a phase diagram of coherence in the $\alpha - (1/R)$ plane, with a large region possessing no coherent firing, abutted by a stripe region (two non-trivial Bragg peaks), which is next to an orthorhombic symmetry phase (four non-trivial Bragg peaks), and then the normal coherent grid cell pattern (six hexagonally arrayed non-trivial Bragg peaks). For cells within the damaged region, the central Bragg peak intensity diminishes uniformly as α is decreased, while it is little affected outside the damaged disk. There is a mathematically required "re-entrance" to the normal phase as $R \rightarrow \infty$. We note that our phases should be observable in fMRI studies of the MEC.

II. METHODS

A. Emergent Grid-like Firing Pattern in a Continuous Attractor Model of a Neuronal Sheet.

In continuous attractor models, each neuron receives inhibitory input from a surrounding ring of local neurons, and the entire network will receive broad-field feed-forward excitation containing location and direction data from elsewhere in the brain. The model, upon integration in a static limit, will tend towards a stable fixed point of the coupled equations or attractor in the full phase space of the coordinates. When the model animal is moving, given sufficiently rapid response of the neurons in the model, the stable firing pattern can flow in response to the motion and this is the origin of the observed grid cell pattern from this picture.

Consider a network of neurons arranged with uniform density on a cortical sheet, and with a connection strength that decreases with distance. If the connections of inhibitory cells extend over a wider range than the connections of excitatory cells, the symmetry is broken, and a population response consisting of a regular pattern of discrete regions of neural activity can be created, arranged on the vertices of a periodic structure. As analyzed in the appendix, the most stable steady state structure in undamaged conditions has hexagonal lattice symmetry.

The dynamics of grid cell activity can be described by the differential equation[23, 24]

$$\tau \frac{ds_i}{dt} = -s_i + f\left(\sum W_{ij} \cdot s_i + B_i\right) . \quad (1)$$

The neural transfer function assumed here, per Burak and Fiete[23], is a simple rectification nonlinearity: $f(x) = x$ for $x > 0$ and 0 otherwise. W_{ij} is the synaptic weight from neuron j to neuron i , which has the character that inhibiting neurons operate at longer range activating ones. Following Burak and Fiete [23], the weight matrix function is written as the difference of two Gaussian curves with different variances which has a “Mexican Hat” shape in position space:

$$W_{ij} = W_0(x_i - x_j - le_{\theta_j}) \quad (2)$$

with

$$W_0(x) = ae^{-\gamma|x|^2} - e^{-\beta|x|^2} . \quad (3)$$

The blue spheres in Fig. 9 represent grid cells in a 2D neuron sheet, corresponding to one of the grid cell layers of the dMEC. For fast simulation, we use a 40×40 neuron sheet, and the coordinates on that 2D plain can be described by a neuron position vector \vec{x}_i , so the weight matrix between i_{th} and j_{th} neurons is actually a function of their separation vector $\vec{x}_i - \vec{x}_j$.

The weight matrix function $W_0(x)$ is the difference of two Gaussians: 1) a is chosen to be 1 to make all the connections inhibitory, which is enough to create grid-like firing pattern while $a > 1$ would not affect the result qualitatively. There is a relative excitatory response at small separation compared to the maximum inhibition. 2) β is used to determine the width of the inhibitory surrounding neuron region. 3) λ is the target periodic wavelength of the formed triangular lattice. Approximately, $\lambda \approx \sqrt{3/\beta}$. 4) For the smaller 40×40 system we take $\gamma = 6.711 \times \beta$ to make the maximum inhibition big enough to generate a grid-like firing pattern for a small dimension lattice. Simulation parameters are in Table 1.

TABLE I. Coefficients Table

a	λ (neurons)	β (1/neuron 2)	γ (1/neuron 2)	l (neurons)	τ (ms)	dt (ms)	η_0	μ
1	8	$3/\lambda^2$	$6.711 \times \beta$	1	10	0.5	0.10315	0.875

B. Grid-like Firing Pattern Flow

The shifted location term $le_{\hat{\theta}_j}$ is associated with the neuron's preferred direction $e_{\hat{\theta}_j}$, and these orientation sensitive firings drive the grid pattern from stationary to flowing. This is a way to mimic the input in the model from the head direction cells. In the head direction system, cells fire selectively with respect to the rat's head orientation as a result of neural integration of head angular velocity signals derived from the vestibular system. In the grid cell system, each neuron receives input from one head-direction cell turned to its preferred direction, and the neuron's outgoing center-surround connectivity profile is not centered on itself, but is shifted by a few neurons along its preferred direction, which is shown in the weight function above as the shifted location vectors. In our grid-like sheet, we tiled the neuron uniformly in this way: each neuron i has a preferred direction (W, E, S, N) , indicated by $e_{\hat{\theta}_i}$, and each 2×2 neuron block contains all four preferred directions.

The feed-forward input to neuron i is:

$$B_i(x) = A_i(x)(1 + \eta_0 e_{\theta_i} \vec{v}) \quad (4)$$

where \vec{v} is the velocity of the rat, in units of m/s . η_0 is the coefficient that characterizes the effects of velocity inputs to the driven pattern flow. $A_i(x)$ is called the *envelope function* which helps to modulate the strength of the input to the neurons. We assume periodic boundary conditions for firing on the sheet, and in this case

$$A_i(x) = 1 \quad (5)$$

If we have a non-zero value for shifted location vector and, then the animal velocity input will drive a flow of the formed pattern. η_0 determined the gain of the velocity response of the network and we need to make sure the term $\eta_0 e_{\theta_j} \vec{v} \ll 1$ so that it can keep the formed lattice is stable.

C. Path Integration

1. Random Walk Generation

A random walk happening within a circular enclosure is used to simulate animals' moving path in real experiments[6]. Here we use the random walk model of Ref.[25]. For the i th step, we have velocity v^i , position r^i , and acceleration a^i . The acceleration is generated using a Gaussian distribution of random variables, with average of zero, standard deviation $\sigma_a^2 = 0.5$ and a mixing coefficient $\mu = 0.875$. The mixing coefficient determines the amount of the current velocity preserved in the next velocity step; this assures a realistically smooth trajectory from which the additional random acceleration boost offers smaller course corrections. We use a small time step $\Delta t = 0.2s$ to make sure the change on rat's trajectory is smooth. The velocity is reflected at the boundary.

$$\begin{cases} v^{i+1} = \mu v^i + a^i \cdot \Delta t & \bar{a} = 0, \bar{a}^2 = \sigma_a^2 \\ r^{i+1} = r^i + v^i \cdot \Delta t \end{cases} \quad (6)$$

2. Path Integration Map

There are N steps in the generated random walk path, and each step contains its velocity v^i and position r^i . We set velocity v^i to be the average velocity from i th step to $(i+1)$ th

step . For each step, the timestep $0.1s$ means updating the neuron sheets' signal 400 times ($0.1s/0.5ms = 200$), and the whole process uses v^i as the velocity input to flow the whole firing pattern. We tracked one single neuron and read its firing rate at position r^i . The position and single tracking neuron firing rate are plotted together showing the single path integration map. This is exactly the same idea of planting electrode measuring activity of a single neuron in a rat's dMEC and tracking the firing signal with the rat's trajectory.[6]

D. Central Damage Model

As discussed in the introduction, Alzheimer's disease affects the hippocampus (place cells) and the entorhinal cortex (grid cells) early and thus disrupts navigation. It may proceed by diffusion of "tau tangles" from cell to cell which will disrupt synaptic function. We focus on one type of damage to the dMEX that can arise from neurodegenerative diseases and affect grid cell performance: diffusing damage that can arise from propagation of neurofibrillary tau tangles similar to the prion diseases[26]. Based on this model, we model neuronal functional loss as a weakening of the output synaptic strength. As we dial the output strength to zero, we effectively "kill" the neuron in the model. In Fig 1c, we show a central diffusion damage on top of the grid-like firing pattern. The 40×40 healthy neuron sheets has its own triangular grids of firing pattern, and then the neurons within the orange region are set to be damaged, after which we can observe neuron signals in different locations(#820 is within the damage region and #400,800,810,1560 are healthy neurons) and with different size of central damage (damage region radius $R = 7$ neurons in Fig 1c).

As a first example, we kill a central neuron and allow the neuronal damage to propagate outward to model the prion like spread alluded to in the above paragraph. The timestep for numerical integration in our simulation is $0.5 ms$ and we take $250 ms$ (500 timesteps) for the surrounding neurons to die. These timescales are obviously significantly accelerated from the AD scale so we can see the effects in a reasonable simulation time frame. The resulting growth speed of the damage cluster radius is 1 neuron/step. We took screenshots every $50 ms$ (100 timesteps) to record the damage as we changed from a circular damage region with a radius of $R = 2$ neurons to $R = 7$ neurons and we made a video of the flow on damaged neuron sheets (Fig. 2e).

Next, we allowed for a nonzero but weakened connection between neurons in the damaged

region and to neurons on the periphery of the undamaged region. A new coefficient α is applied to describe the damage: $W_{damage} = \alpha W_{health}$ ($0 \leq \alpha \leq 1$). For those neurons lie in the circular damaged region, their presynapse W_{ij} and postsynapse W_{ji} are not same anymore, and we assume postsynapse (from damaged neurons to healthy neurons) shall be smaller than presynapse (from health neurons to damaged neurons).

$$\begin{cases} W_{ij} = W_{ji} = W_0(i > R, j > R) \\ W_{ij} = \alpha W_{ji} = \alpha W_0(i < R, j > R) \\ W_{ij} = W_{ji} = \alpha W_0(i < R, j < R) \end{cases} \quad (7)$$

When two neurons are both healthy, their connection weight W_{ij} and W_{ji} are the same and are given in equation ??; when one neuron is damaged, we assume it can still accept the signal from other neurons with no reduction but that the signal sent from it will be weaker, this is a more realistic assumption than simply killing the neuron. We affect this by multiplying the weights by α for all neuronal outputs emerging from within the damaged region. Note that $\alpha=0$ corresponds to dead neurons.

III. RESULTS AND DISCUSSION

A. Linear Grid Pattern Flow/Velocity Relationship in Healthy/Damaged Models

We employ 40×40 neuron sheets to simulate one layer of the dMEC, with real neuron number about $10^3 - 10^5$). We start the stimulation with small random noise within the range from -0.1 to 0.1 (arbitrary units, but referenced to the static background input of 1), (Fig 2a), then apply the aperiodic boundary condition for a $250ms$ stimulation process (same as 500 timesteps). For shorter times, we see randomly separated big firing blobs emerge on the inactivated black background (Fig 2b), and the central activity is higher than the surroundings. Then as we run another $250ms$ simulation under periodic boundary conditions. we develop a complete periodic lattice of firing blobs (Fig 2c). All the simulations above are done with zero velocity input, and that explains why the firing regions are small radius “blobs” instead of the peaks clusters(shown in Fig 2d). Then we let the whole neuron sheet complete building triangular lattice using “healing process”: Apply a nonzero velocity input ($0.8m/s$) in three directions $(0, \pi/5, \pi/2 - \pi/5)$, and complete $500ms$ simulation for each of directions. The “healing process” will cure the defects and generate completed

triangular lattice (Fig 2d)

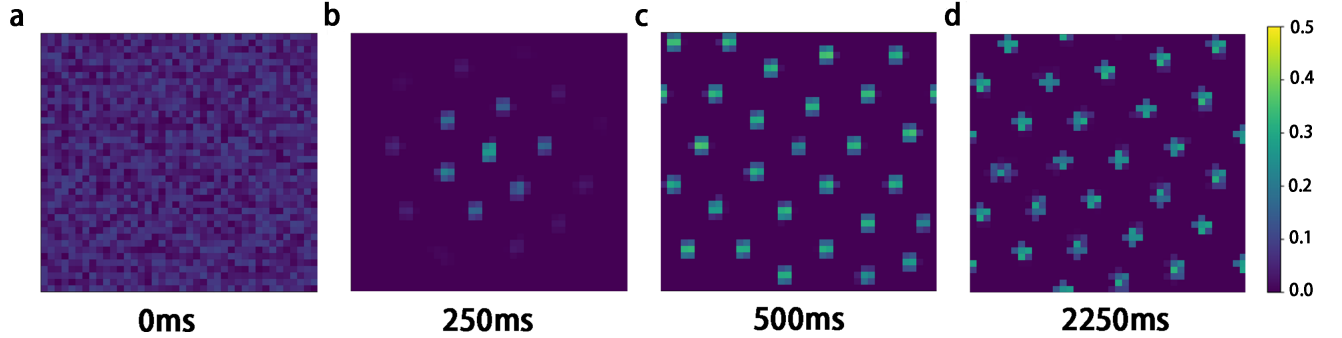


FIG. 2. Temporal emergence of Firing Patterns for undamaged and damaged grid cell layer. (a) Initial state of neuron sheet includes a random noise signal ranging from -0.1 to 0.1. (b) The aperiodic boundary condition shapes the neuronal signal pattern to generate grids in the first 250ms, beginning with an intense central peak with weaker surrounding peaks. (c) Change boundary condition from aperiodic to periodic expands the grids evenly. (d) Non-zero velocity inputs ($0.8m/s$ in three directions) heal the defects of previous grids and generate a hexagonal lattice of grid firing peaks. Figures (a) (d) are heatmaps with the same colorbar.

The dynamics of the firing patterns are associated with velocity input \vec{v} . The velocity input, used in the feedback function $\mathbf{B}(\vec{v})$ of the firing rate equation (1), is the animal's moving velocity in real experiments. This velocity changes its direction and magnitude when animal runs^[18], which helps us get the actual path information into our future path integration calculation. With zero velocity input, all the firing peaks will be on vertices of a stationary hexagonal lattice. With nonzero velocity input, the model input with direction sensitive cells tiling the grid cell layer initiates a flow of the firing signal, in the opposite direction to velocity input \vec{v} . The linear relationship between the flow speed and velocity input \vec{v} is very important to generate the later accurate path integration (Figure 3a). We introduce the scaling ratio \mathbf{K} to describe the relationship:

$$\text{flowing speed} = \mathbf{K} \cdot |\vec{v}| \quad (8)$$

Fig 3 shows that for both dead neurons and damaged ones that the whole driving pattern continues, bypassing the damage. The healthy neurons will still fire normally, while the damaged neurons will be fully muted or at least weaker in excitatory response. The firing

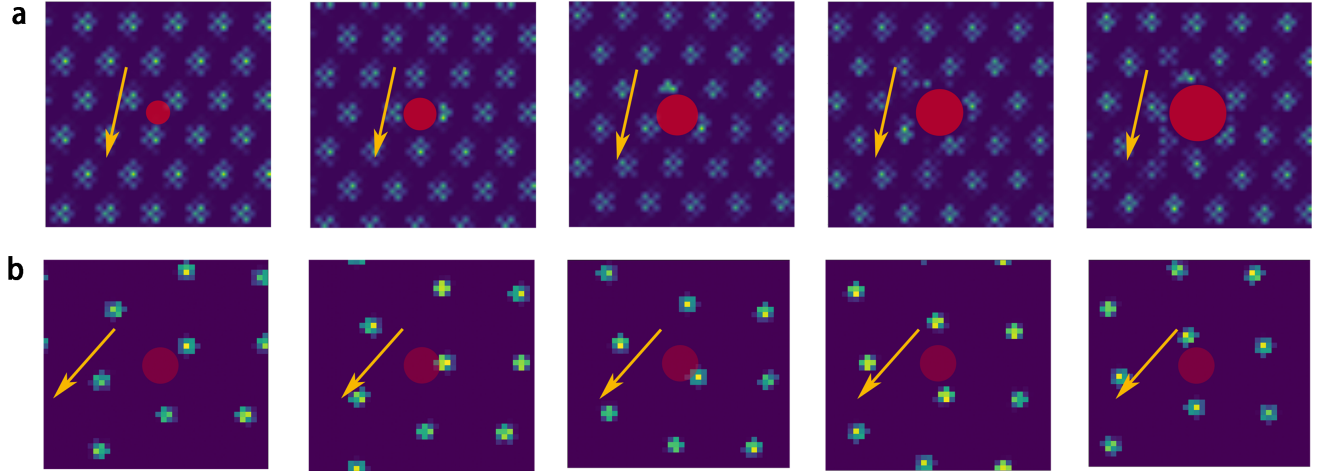


FIG. 3. Neuron Sheet Firing Pattern with Model Damage. (a) Dead neurons ($\alpha=0$) in the red damaged regions, with successive damage region radii of 2,4,6,8 neurons. Yellow arrows indicate the flow direction in the opposite direction of the animal velocity, with grid cell firing peaks bypassing the central damage even as it grows. (b) Weakend neuronal firing in the central damage region (red), with $R = 4$ neurons and $\alpha = 0.6$,The whole grid-like firing pattern is moving along the yellow direction, and neurons fire (more weakly) in the damaged region.

pattern of healthy neurons is not strongly influenced by damaged ones, and still shows stability with flow. We examine the relationship between flow speed and velocity input for both healthy neuron sheets and the damaged one.

Fig 4a shows both healthy and damaged neurons sheets retain the linear relationship between flow speed and velocity input \vec{v} , a huge damaged neuron cluster like the central damaged one ($R = 7$ neurons) is pretty big in our 40 by 40 neuron sheets, but the proportional relationship between flow speed and physical speed \vec{v} is still close to those of the undamaged neuron sheet. The firing pattern flow is also stable regardless of velocity input direction or damage size. In figure 4b, we show velocity inputs in different directions and magnitudes, and the damage doesn't influence the linear relationship. And in figure 4c, We increase the central damage region from $R = 0$ neuron to $R = 8$ neurons, and compare their flow speed under the velocity inputs of the same magnitude but different directions ($\pi/4, \pi/2, 3\pi/4$), The overlap of lines indicates, with the same amplitude of velocity input,that the velocity direction doesn't dramatically influence the firing pattern flow. The linear relationship is stable regardless of damage size or velocity inputs.

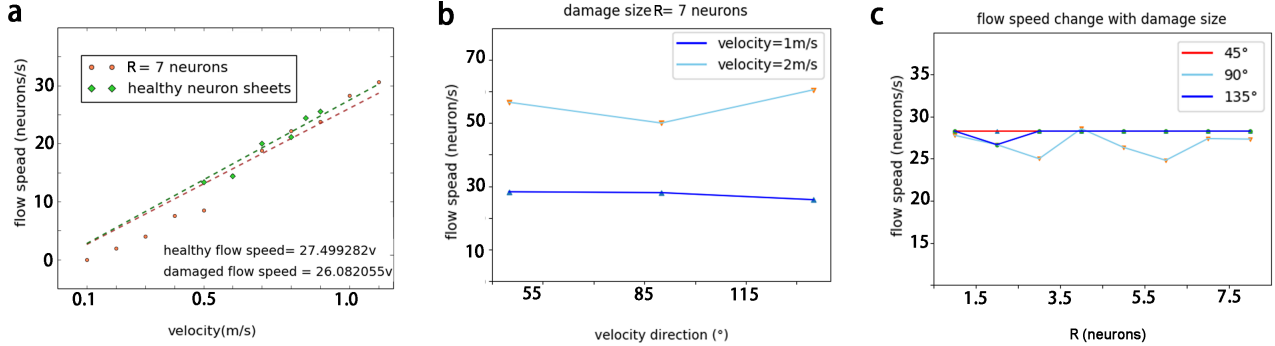


FIG. 4. Relationship of Firing Peak Flow Speed and Velocity Input. (a) Linear relationship of flow speed and magnitude of velocity input, in both healthy neuron sheets and damaged neuron sheets. (b) Stability of linear relationship under different velocity inputs for a damaged sheet with dead neurons. There are six different velocity inputs (1 m/s and 2 m/s) in directions $(\pi/4, \pi/2, 3\pi/4)$, and the linear relationship is stable under the same size of damage region (damage radius $R = 7$ neurons, $\alpha=0$). (c) Stability of linear relationship under different damage sizes. The velocity input is 1 m/s in three directions $(\pi/4, \pi/2, 3\pi/4)$, and the central damage size increases from $R = 1$ to $R = 8$ neurons, with the central neurons dead ($\alpha = 0$). The overlapping of horizontal lines indicates the flow speeds are the same if the velocity inputs' magnitudes are the same, regardless of the change of damage size or velocity direction.

B. Path Integration Map for the Healthy Neuron Model

In one simulation path, each step contains four elements: the animal(rat)'s position vector (x, y) and velocity vector (v_x, v_y) . We put the rat's velocity vector as a velocity input \vec{v} into the steady state grid cell flow, and the output results show us rat's single grid cell's firing rate at that position. Now the animal's firing rate of one tracking neuron is linked with its position within the enclosure, which can be plotted as our path-integration-based map (Fig.5).

From the single path integration simulation, we found the firing pattern shows weak grids, more like discrete highlight dots separated in a grid pattern (Fig 4a). To achieve a more accurate and clear result, we use the average of five different path integration, for each of them, the same tracking neuron signal starts with the same firing pattern at the very beginning, but follows different trajectories. We add the five sets of firing rate together to generate the path integration map. In Fig 5b, we can see the average path integration map

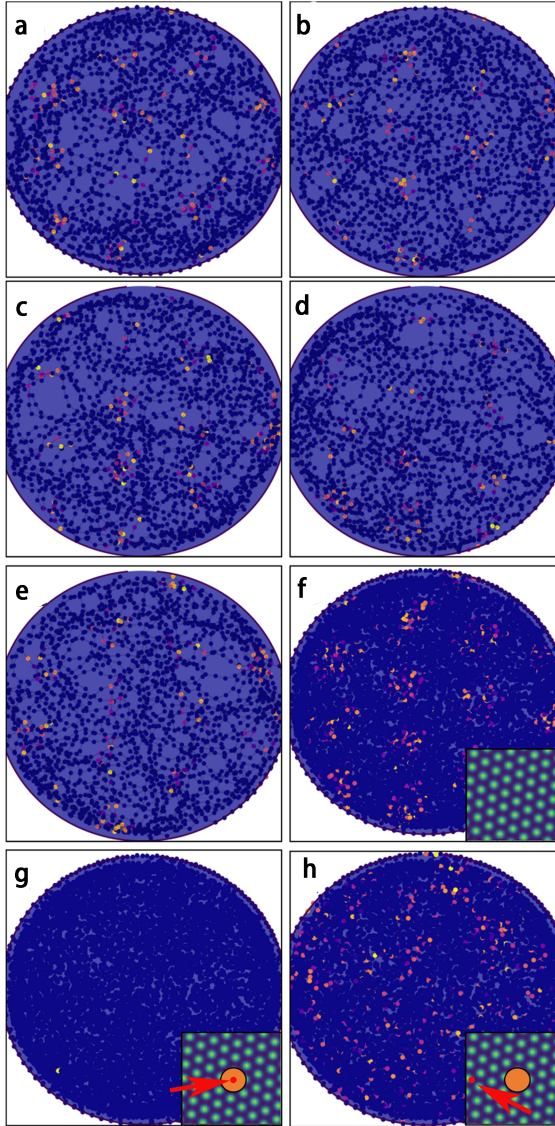


FIG. 5. Single Path Integration Map and Average Path Integration Maps of Healthy/Damaged Neuron Sheets. (a) (e), Single path integration map of healthy neuron sheets for five different trajectories. (f) Average path integration map of the above five shows a clear triangular grid pattern. (g) The firing of a dead neuron (neuron #820) is muted in path integration map. (h) Firing of a healthy neuron (neuron #800) doesn't generate a grid -like average path integration map with damage (damage model region $R = 7$ neurons, $\alpha=0$)

present better grids pattern compared with single path integration map.

When we replaced the healthy neuron sheets with the damaged neuron sheet model, even though damage does not destroy the signal's flow stability, it influences the path integration

in terms of degrading the triangular lattice firing pattern in the random walk on the two dimensional area. In Fig 5c & 5d, we found the damage of killing neurons brought us the worst influence, even a very small region of dead cells can totally destroy the grid from generating. Tracking the dead neuron in the damaged region (Fig 5c) shows no firing signal all along the path, the healthy neuron outsider the damaged region are strongly influenced by the damage and cannot generate triangular grids like Fig 5b.

C. Fourier Transformation Analysis and Damage Phase Diagram

We found small damage region and big damage coefficient α can lead to stable grids, even though too big damage region size (radius over 7 neurons) or too small damage coefficient α ($\alpha < 0.2$) still prevent the grids from generating. Figure 1c is a simplified model of 2D 40 by 40 neuron sheet with central damage $R = 7$ neurons, and tracking neuron #.800 is outside the damage region while #820 is within the region. We crop the center square region of path integration map to eliminate boundary effects, and do the discrete Fourier Transformation (DFT) on the truncated position space. For those trajectories with clear enough hexagonal grid structure, the DFT diagrams show six Bragg peaks around the center (Fig 6a), and those without grids show only one central peak corresponding to the average firing (Fig 6d). Between these extremes, we find regions with striped firing (2 non-zero Bragg peaks) and orthorhombic firing (4 non zero Bragg peaks anisotropic in the plain) (Fig 6b & 6c).

By studying the non-zero Bragg peaks as a function of $1/R, \alpha$ we can generate the phase diagram shown in (Fig 7a & 7b). The phase diagrams of both are similar in detail, but the discrete Fourier Transformation (DFT) central peak intensities varies. Fig 7c is the contour diagram of DFT central peak intensity for neuron within/outside the damage region. For neuron outside the damage region (#800), the peak intensity is higher and more or less constant in amplitude with increased damage size and strength, while for a neuron in the damaged region (#820) the central peak intensity diminishes. This peak measures the average firing over the space of the 2-D enclosure.

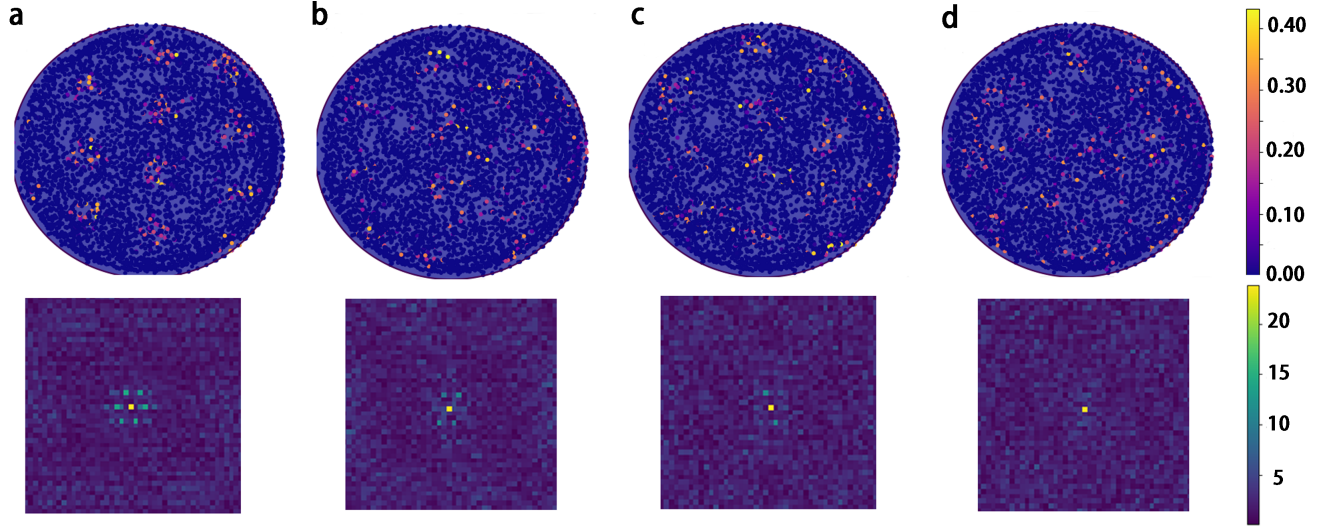


FIG. 6. Average Path Integration Map with Model Damage and Discrete Fourier Transform (DFT). (a) For neuron #800, damage coefficient $\alpha = 1$, which is a healthy neuron sheets, the associated average path integration map shows clear triangular grids. DFT diagram has a hexagonal structures of 6 peaks around the center. (b) Neuron #800, damage coefficient $\alpha = 0.5$, damage radius $R = 4$ neurons. DFT diagram has 4 peaks around the center. (c) Neuron #820, damage coefficient $\alpha = 0.3$, damage radius $R = 2$ neurons. DFT diagram has 2 peaks around the center. (d) Neuron #800, damage coefficient $\alpha = 0.4$, damage radius $R = 4$ neurons. DFT diagram has 0 peaks around the center. Average path integration maps in (b),(c),(d) are regraded as none-grids path integration map.

IV. CONCLUSION

By studying the Bragg peaks in the Fourier Transformed pattern of position space firing fields for model grid cells, we have shown that damage to a model grid cell layer as parameterized by reduced synaptic output strength α and damage radius R leads to a predictable sequence of reduced grid cell firing symmetry from hexagonal lattice, to orthorhombic lattice, to stripes, and on to no coherent pattern (single central peak). We find that the central Bragg peak in the region with no coherent grid structure is largely unchanged for grid cells outside the damaged region, but strongly reduced for grid cells in the damaged region. For large area damage, there is a re-entrant transition to the fully hexagonal grid structure. The modifications of firing patterns associated with the less ordered structures should be visible in fMRI experiments which can pick up the full six fold symmetric firing pattern in

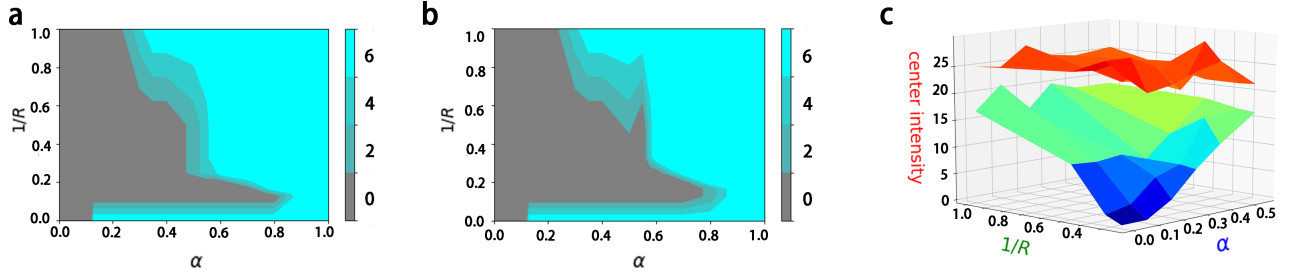


FIG. 7. Phase Diagrams and Fourier Transform Central Peak Intensity. (a) For neuron #800 phase diagrams of grid cell order in the $1/R$ - α plane. In the teal region we find hexagonal lattice grids in the average path integration map; in the charcoal region there are no grids in the average path integration map region. The two other shaded regions between teal and charcoal correspond to a striped a grid (2 peaks in the DFT), an orthorhombic grid (4 peaks in the DFT). For $1/R = 0$, all neurons are damaged α , and for $1/R = \infty$ or $\alpha = 1$ all neurons are healthy. (b) Firing phase diagrams for neuron #820 phase diagrams in the $1/R$ - α plane. The structure is nearly the same as the phase diagram in (a). (c) DFT central peak intensity as a function of $1/R$ and α for undamaged and damaged cells in the region without coherent grid cell firing (charcoal area in (a),(b)). The surface is for the healthy neuron #800 (healthy neurons), and the bottom surface is for the #820 (damaged neuron). Damaged neurons have weak firing signal and bigger variance with changing of $1/R$ and α .

the dMEC. This makes for an important tool in assessing potentially the level of synaptic damage associated with neurodegenerative diseases such as Alzheimer's, that may allow for early diagnosis and the use of small molecule aggregation inhibitor treatments such as anle138b[27, 28].

ACKNOWLEDGMENTS

We acknowledge useful conversations with M. Zaki Jawaid at the start of the project and with Rishidev Chaudhuri about the origin of flow of the firing peaks with motion.

Appendix A: Influence of Time Steps dt for Accelerating Simulation

To improve simulation's effectiveness, we found the time steps dt play a big part in simulation speed. A bigger time steps dt means less numerical simulating cycles within the same period of time. A small time step dt can improve the simulations accuracy while some small time steps are enough to generate the hexagonal grid structure. We find that $dt = 0.5, 1.0, 2.0 \text{ ms}$ can each generate a hexagonal lattice grid for long enough trajectory as shown in Fig 8. Accordingly we sacrifice some accuracy for better simulation speed by choosing larger dt , which can still get us good results for average path integration maps.

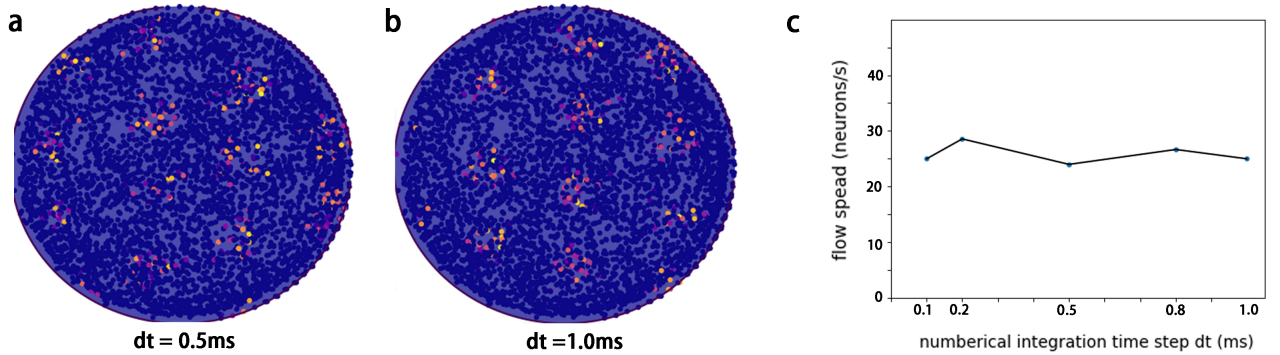


FIG. 8. **Influence of time step size dt on simulations.** (a) Average path integration map of Neuron # 800, healthy grids, $dt = 0.5\text{ms}$. (b) Neuron # 800, healthy grids, $dt = 1.0\text{ms}$. (c) different time steps $dt = 0.1\text{ms}, 0.2\text{ms}, 0.5\text{ms}, 0.8\text{ms}, 1.0\text{ms}$ don't affect the flowing speed when velocity inputs are the same ($\vec{v} = 1\text{m/s}$)

Appendix B: Explanation of flow determined by preferred direction $e_{\hat{\theta}_j}$ and shifted location vectors $le_{\hat{\theta}_j}$

The grid cells can create a grid like firing pattern without the shifted location vectors $le_{\hat{\theta}_j}$, but $le_{\hat{\theta}_j}$ is the key to generate a steady firing pattern flow. The addition of $le_{\hat{\theta}_j}$ breaks the symmetry of weight matrix W to make $W_{ij} \neq W_{ji}$ between two neurons. In Fig 9a, all the neuron have the same preferred direction $e_{\hat{\theta}_j}$ to the right, and the new weight matrix $W_{ij}(x_i - x_j - le_{\hat{\theta}_j})$ is bigger in magnitude than $W_{ji}(x_j - x_i - le_{\hat{\theta}_i})$ considering $le_{\hat{\theta}_i} = le_{\hat{\theta}_j}$. Because weight matrix is negative, the connection along the preferred direction has bigger inhibitory affects than the connection in the opposite direction, which drives the grid-like

firing pattern move opposite the preferred direction. When neuron groups with different preferred directions e_{θ_j} work together evenly, the symmetry of weight matrix can be restored and that explains why there is a static firing pattern when velocity input is zero (Fig 2c). When the velocity input is nonzero, it can strongly activate the neurons that share the same preferred direction, which drives the grid-like firing pattern to flow in the opposite direction to the velocity.

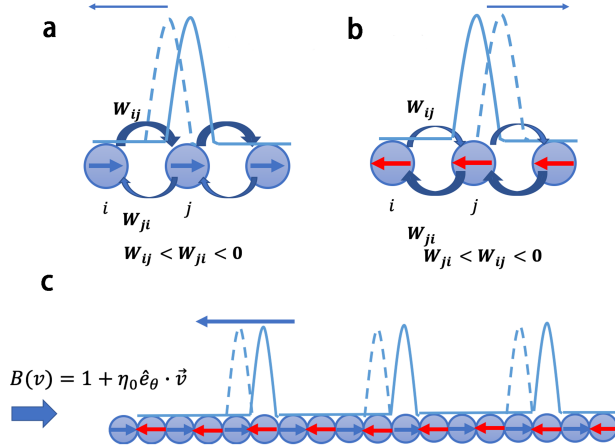


FIG. 9. **1D Grid cell Model with Preferred Direction.** (a) Neurons have preferred direction pointing to the right, breaking the symmetry of weight matrix ($W_{ij} < W_{ji} < 0$), the inhibitory connection to left is bigger than that to the right, which drives the grids firing pattern to move to the left. The blue arrow indicates driving flow direction, the solid blue curve is current firing pattern and the dashed curve indicates the firing signal the next moment. (b) Neurons with preferred direction pointing to the left drive the flow pointing to the right. (c) neurons with different preferred directions work together evenly make the grid-like pattern stationary, and with non-zero velocity input pointing to the left (big blue arrow) will drive the grids to flow to the left.

Appendix C: mean field analysis to explain triangular grids

The firing rate equations for Burak and Fiete are:

$$\tau \frac{ds_i}{dt} = -s_i + f(\sum W_{ij} \cdot s_j + B_i) \quad (C1)$$

where:

$$W_{ij} = a \cdot \exp(-\gamma |\vec{x}_i - \vec{x}_j|) - \exp(-\beta |\vec{x}_i - \vec{x}_j|) \quad (C2)$$

With $w_{ij} < 0$ uniformly and $s_i > 0, B = 1$. That is particularly no region of s_i space where the argument of the rectification in (C1) is negative hence (C1) is always in the linear regime.

The fixed point is set by the condition

$$\frac{ds_i}{dt} = 0 \quad (C3)$$

with $s_i = \sum W_{ij} \cdot s_i + B$ which can be viewed as the solution arising from minimizing the "cost function"

$$C(s_i) = \frac{1}{2} \sum s_i^2 - \sum B \cdot s_i - \frac{1}{2} s_i W_{ij} s_j \quad . \quad (C4)$$

Fourier transformation of the firing rates is given by

$$s_i = \frac{1}{\sqrt{N}} \sum \tilde{s}(\tilde{q}) e^{-i \cdot \tilde{q} \cdot \vec{r}_i} \quad (C5)$$

\vec{r}_i is the neuron position in $N \times N$ sheets; $\vec{r}_i + N\hat{x} = \vec{r}_i + N\hat{y} = \vec{r}_i$. $\tilde{q} \subset [q_x, q_y], -\frac{\pi(N-1)}{N} \leq q_\alpha \leq \pi, \alpha = x, y$. where

$$\tilde{W}(\tilde{q}) = a \frac{\pi}{\gamma} e^{-\frac{q^2}{4\gamma}} - \frac{\pi}{\beta} e^{-\frac{q^2}{4\beta}} \quad (C6)$$

With $\tilde{W}(\tilde{q}) > 1$, an instability at finite \tilde{q} is possible. $\tilde{W}(0) = a \frac{\pi}{\gamma} - \frac{\pi}{\beta}$, and $\tilde{W}(\tilde{q})$ is maximum when $\tilde{q}_0 = 2\sqrt{2(\frac{\beta\gamma}{\gamma-\beta}) \ln(\frac{\gamma}{\beta})}$. $a = 1$.

We can assume different solutions of the form

$$s_i(\vec{r}) = a_i [1 + b_i \sum f_i(\tilde{q}_k \cdot \vec{r})] \quad (C7)$$

where $|\tilde{q}_k| = q_0$, and there are constraints:

- (1) $1 + b_i \sum f_i(\tilde{q}_k \cdot \vec{r}) \geq 0$
- (2) $f_i(\tilde{q}_k \cdot \vec{r})$ must be periodic.

Examples are:

- (1) $s_0(\vec{r}) = a_0$, uniformly.
- (2) $s_1(\vec{r}) = a_1 [1 + \cos(q_0 x)]$, periodical along x direction.
- (3) $s_2(\vec{r}) = a_2 [1 + \frac{1}{2} \cos(q_0 x) + \frac{1}{2} \cos(q_0 y)]$, rectangle grids.
- (4) $s_3(\vec{r}) = a_3 [1 + \frac{2}{3} \cos(\vec{q}_1 \cdot \vec{r}) + \frac{2}{3} \cos(\vec{q}_2 \cdot \vec{r}) + \frac{2}{3} \cos(\vec{q}_3 \cdot \vec{r})]$, triangular grids.

where $\vec{q}_1 = q_0(1, 0), \vec{q}_2 = q_0(-\frac{1}{2}, \frac{\sqrt{3}}{2}), \vec{q}_3 = q_0((-\frac{1}{2}, -\frac{\sqrt{3}}{2}))$.

And their Fourier Transforms are

- (1) $\tilde{s}_0(\tilde{q}) = a_0 \delta_{\tilde{q},0}$
- (2) $\tilde{s}_1(\tilde{q}) = a_1 [\delta_{\tilde{q},0} + \frac{1}{2}(\delta_{\tilde{q},q_0x} + \delta_{\tilde{q},-q_0x})]$
- (3) $\tilde{s}_2(\tilde{q}) = a_2 [\delta_{\tilde{q},0} + \frac{1}{4}(\delta_{\tilde{q},q_0x} + \delta_{\tilde{q},-q_0x} + \delta_{\tilde{q},q_0y} + \delta_{\tilde{q},-q_0y})]$
- (4) $\tilde{s}_3(\tilde{q}) = a_3 [\delta_{\tilde{q},0} + \frac{1}{3}(\delta_{\tilde{q}_1 \cdot \vec{r}} + \delta_{-\tilde{q}_1 \cdot \vec{r}} + \delta_{\tilde{q}_2 \cdot \vec{r}} + \delta_{-\tilde{q}_2 \cdot \vec{r}} + \delta_{\tilde{q}_3 \cdot \vec{r}} + \delta_{-\tilde{q}_3 \cdot \vec{r}})]$

Substituting these in the cost function yields the results

$$C[\tilde{S}_{\tilde{q}}] = \frac{1}{2} \sum_{\tilde{q}} |\tilde{s}(\tilde{q})|^2 [1 - \tilde{W}(\tilde{q})] - \sqrt{N} B \tilde{s}(\tilde{q} = 0) \quad (\text{C8})$$

- (1) $C_0 = -\sqrt{N} B a_0 + \frac{a_0^2}{2} [1 - \tilde{W}(0)]$
- (2) $C_1 = -\sqrt{N} B a_1 + \frac{a_1^2}{2} \{[1 - \tilde{W}(0)] + \frac{1}{2}[1 - \tilde{W}(q_0)]\}$
- (3) $C_2 = -\sqrt{N} B a_2 + \frac{a_2^2}{2} \{[1 - \tilde{W}(0)] + \frac{1}{4}[1 - \tilde{W}(q_0)]\}$
- (4) $C_3 = -\sqrt{N} B a_3 + \frac{a_3^2}{2} \{[1 - \tilde{W}(0)] + \frac{2}{3}[1 - \tilde{W}(q_0)]\}$

We can summarize these results as

$$C_i = -\sqrt{N} B a_i + \frac{a_i^2}{2} \{[1 - \tilde{W}(0)] + \sigma_i [1 - \tilde{W}(q_0)]\} \quad (\text{C9})$$

Introduce:

$$\rho_i = [1 - \tilde{W}(0)] + \sigma_i [1 - \tilde{W}(q_0)] \quad (\text{C10})$$

Equation (C9) can be changed into:

$$C_i = \frac{\rho_i}{2} \left(a_i - \frac{\sqrt{N} B}{\rho_i} \right)^2 - \frac{N B^2}{2 \rho_i} \quad (\text{C11})$$

$$C_{i,min} = -\frac{N B^2}{2 \rho_i} \quad \text{when } a_i = \frac{\sqrt{N} B}{\rho_i}. \quad (\text{C12})$$

For 40×40 neuron sheets with $a = 1$, $N = 1600$, $B = 1$, $\gamma = 6.7 \times \beta$, $\beta = \frac{3}{64}$; We have $\tilde{q}_0 = 0.916$, and $\tilde{W}(0) = -57.02$, $\tilde{W}(\tilde{q}_0) = 4.37$.

- (1) $C_{0,min} = -13.79$, $a_0 = 0.689$
- (2) $C_{1,min} = -14.20$, $a_1 = 0.71$
- (3) $C_{2,min} = -13.99$, $a_2 = 0.6995$
- (4) $C_{3,min} = -14.34$, $a_3 = 0.7172$

Notice that the hexagonal grid shows the lowest cost, indicating it is more stable than grid structures.

- [1] J. O’Keefe and L. Nadel, *The hippocampus as a cognitive map* (Oxford: Clarendon Press, 1978).
- [2] G. M. Muir and D. K. Bilkey, Instability in the place field location of hippocampal place cells after lesions centered on the perirhinal cortex, *Journal of Neuroscience* **21**, 4016 (2001).
- [3] L. L. Chen, L.-H. Lin, E. J. Green, C. A. Barnes, and B. L. McNaughton, Head-direction cells in the rat posterior cortex, *Experimental brain research* **101**, 8 (1994).
- [4] J. S. Taube, R. U. Muller, and J. B. Ranck, Head-direction cells recorded from the postsubiculum in freely moving rats. i. description and quantitative analysis, *Journal of Neuroscience* **10**, 420 (1990).
- [5] J. D. Seelig and V. Jayaraman, Neural dynamics for landmark orientation and angular path integration, *Nature* **521**, 186 (2015).
- [6] T. Hafting, M. Fyhn, S. Molden, M.-B. Moser, and E. I. Moser, Microstructure of a spatial map in the entorhinal cortex, *Nature* **436**, 801 (2005).
- [7] B. L. McNaughton, F. P. Battaglia, O. Jensen, E. I. Moser, and M.-B. Moser, Path integration and the neural basis of the ‘cognitive map’, *Nature Reviews Neuroscience* **7**, 663 (2006).
- [8] A. Mudher and S. Lovestone, Alzheimer’s disease—do tauists and baptists finally shake hands?, *Trends in neurosciences* **25**, 22 (2002).
- [9] M. Goedert, M. Spillantini, and R. Crowther, Tau proteins and neurofibrillary degeneration, *Brain pathology* **1**, 279 (1991).
- [10] W. Chun and G. Johnson, The role of tau phosphorylation and cleavage in neuronal cell death., *Frontiers in bioscience: a journal and virtual library* **12**, 733 (2007).
- [11] J. W. Wilesmith, G. Wells, M. P. Cranwell, and J. Ryan, Bovine spongiform encephalopathy: epidemiological studies., *The Veterinary Record* **123**, 638 (1988).
- [12] C. Casalone and J. Hope, Atypical and classic bovine spongiform encephalopathy, in *Handbook of clinical neurology*, Vol. 153 (Elsevier, 2018) pp. 121–134.
- [13] C. Darwin, *Origin of certain instincts* (1873).
- [14] B. De Strooper and E. Karan, The cellular phase of alzheimer’s disease, *Cell* **164**, 603 (2016).

[15] E. N. Cline, M. A. Bicca, K. L. Viola, and W. L. Klein, The amyloid-beta oligomer hypothesis: Beginning of the third decade, *Journal of Alzheimers Disease* **64**, S567 (2018).

[16] G. W. Van Hoesen, B. T. Hyman, and A. R. Damasio, Entorhinal cortex pathology in alzheimer's disease, *Hippocampus* **1**, 1 (1991).

[17] L. Kunz, T. N. Schroeder, H. Lee, C. Montag, B. Lachmann, R. Sariyska, M. Reuter, R. Stirnberg, T. Stoecker, P. C. Messing-Floeter, J. Fell, C. F. Doeller, and N. Axmacher, Reduced grid-cell-like representations in adults at genetic risk for alzheimer's disease, *Science* **350**, 430 (2015).

[18] M. Stangl, J. Achtzehn, K. Huber, C. Dietrich, C. Tempelmann, and T. Wolbers, Compromised grid-cell-like representations in old age as a key mechanism to explain age-related navigational deficits, *Current Biology* **28**, 1108 (2018).

[19] H. Zempel, J. Luedtke, Y. Kumar, J. Biernat, H. Dawson, E. Mandelkow, and E. M. Mandelkow, Amyloid-beta oligomers induce synaptic damage via tau-dependent microtubule severing by *ttll6* and *spastin*, *Embo Journal* **32**, 2920 (2013).

[20] Y. Chen, L. Liu, M. Li, E. Yao, J. Hao, Y. Dong, X. Zheng, and X. Liu, Expression of human tau40 in the medial entorhinal cortex impairs synaptic plasticity and associated cognitive functions in mice, *Biochemical and Biophysical Research Communications* **496**, 1006 (2018).

[21] H. Fu, G. A. Rodriguez, M. Herman, S. Emrani, E. Nahmani, G. Barrett, H. Y. Figueroa, E. Goldberg, S. A. Hussaini, and K. E. Duff, Tau pathology induces excitatory neuron loss, grid cell dysfunction, and spatial memory deficits reminiscent of early alzheimer's disease, *Neuron* **93**, 533 (2017).

[22] X. Yang, C. Yao, T. Tian, X. Li, H. Yan, J. Wu, H. Li, L. Pei, D. Liu, Q. Tian, L. Q. Zhu, and Y. Lu, A novel mechanism of memory loss in alzheimer's disease mice via the degeneration of entorhinal-ca1 synapses, *Molecular Psychiatry* **23**, 199 (2018).

[23] Y. Burak and I. R. Fiete, Accurate path integration in continuous attractor network models of grid cells, *PLoS Comput Biol* **5**, e1000291 (2009).

[24] P. Dayan, L. F. Abbott, *et al.*, Theoretical neuroscience: computational and mathematical modeling of neural systems, *Journal of Cognitive Neuroscience* **15**, 154 (2003).

[25] A. V. Samsonovich and G. A. Ascoli, A simple neural network model of the hippocampus suggesting its pathfinding role in episodic memory retrieval, *Learning & Memory* **12**, 193 (2005).

[26] G. F. Hall and B. A. Patuto, Is tau ready for admission to the prion club?, *Prion* **6**, 223 (2012).

[27] L. Antonschmidt, R. Dervisoglu, S. Ryazanov, A. Leonov, M. Wegstroth, K. Giller, S. Becker, J. Lee, R. Lal, G. Eichele, A. Fischer, A. Giese, L. Andreas, and C. Griesinger, The small molecule anle138b shows interaction with alpha-synuclein oligomers in phospholipid membranes, *Biophysical Journal* **114**, 560A (2018).

[28] L. Antonschmidt, R. Dervisoglu, S. Ryazanov, A. Leonov, M. Wegstroth, K. Giller, S. Becker, R. Benz, G. Eichele, A. Fischer, A. Giese, L. Andreas, and C. Griesinger, Protein-drug interactions in the membrane: The small molecule anle138b and its binding to alpha-synuclein oligomers, *Biophysical Journal* **116**, 352A (2019).

[29] N. Nathanson, J. Wilesmith, and C. Griot, Bovine spongiform encephalopathy (bse): causes and consequences of a common source epidemic, *American journal of epidemiology* **145**, 959 (1997).

[30] A. M. Turing, The chemical basis of morphogenesis, *Bulletin of mathematical biology* **52**, 153 (1990).

[31] E. Kropff and A. Treves, The emergence of grid cells: Intelligent design or just adaptation?, *Hippocampus* **18**, 1256 (2008).

[32] V. Balasubramanian, Heterogeneity and efficiency in the brain, *Proceedings of the IEEE* **103**, 1346 (2015).

[33] J. Widloski and I. R. Fiete, A model of grid cell development through spatial exploration and spike time-dependent plasticity, *Neuron* **83**, 481 (2014).

[34] P. E. Welinder, Y. Burak, and I. R. Fiete, Grid cells: the position code, neural network models of activity, and the problem of learning, *Hippocampus* **18**, 1283 (2008).

[35] I. R. Fiete, Y. Burak, and T. Brookings, What grid cells convey about rat location, *Journal of Neuroscience* **28**, 6858 (2008).

[36] L. Pini, M. Pievani, M. Bocchetta, D. Altomare, P. Bosco, E. Cavedo, S. Galluzzi, M. Mazzoni, and G. B. Frisoni, Brain atrophy in alzheimer's disease and aging, *Ageing Research Reviews* **30**, 25 (2016).

[37] G. C. Ruben, T. L. Ciardelli, I. GrundkeIqbal, and K. Iqbal, Alzheimer disease hyperphosphorylated tau aggregates hydrophobically, *Synapse* **27**, 208 (1997).

[38] E. Sipos, A. Kurunczi, A. Kasza, J. Horvath, K. Felszeghy, S. Laroche, J. Toldi, A. Parducz,

B. Penke, and Z. Penke, beta-amyloid pathology in the entorhinal cortex of rats induces memory deficits: Implications for alzheimer's disease, *Neuroscience* **147**, 28 (2007).

[39] B. Zhang, J. Carroll, J. Q. Trojanowski, Y. M. Yao, M. Iba, J. S. Potuzak, A. M. L. Hogan, S. X. Xie, C. Ballatore, A. B. Smith, V. M. Y. Lee, and K. R. Brunden, The microtubule-stabilizing agent, epothilone d, reduces axonal dysfunction, neurotoxicity, cognitive deficits, and alzheimer-like pathology in an interventional study with aged tau transgenic mice, *Journal of Neuroscience* **32**, 3601 (2012).